

TIDALLY INDUCED BARS IN DWARF GALAXIES ON DIFFERENT ORBITS AROUND A MILKY WAY-LIKE HOST

GRZEGORZ GAJDA^{1,2}, EWA L. LOKAS¹ AND E. ATHANASSOULA²

¹Nicolaus Copernicus Astronomical Center, Polish Academy of Sciences, Bartycka 18, 00-716 Warsaw, Poland

²Aix Marseille Univ, CNRS, LAM, Laboratoire d’Astrophysique de Marseille, Marseille, France

ABSTRACT

Bars in galaxies may develop through a global instability or due to an interaction with another system. We study bar formation in disk dwarf galaxies orbiting a Milky Way-like galaxy. We employ N -body simulations to study the impact of initial orbital parameters: the size of the dwarf galaxy orbit and the inclination of its disc with respect to the orbital plane. In all cases a bar develops in the center of the dwarf during the first pericenter on its orbit around the host. Between subsequent pericenter passages the bars are stable, but at the pericenters they are usually weakened and shortened. The initial properties and details of the further evolution of the bars depend heavily on the orbital configuration. We find that for the exactly prograde orientation, the strongest bar is formed for the intermediate-size orbit. On the tighter orbit, the disc is too disturbed and stripped to form a strong bar. On the wider orbit, the tidal interaction is too weak. The dependence on the disc inclination is such that weaker bars form in more inclined discs. The bars experience either a very weak buckling or none at all. We do not observe any secular evolution, possibly because the dwarfs are perturbed at each pericenter passage. The rotation speed of the bars can be classified as slow ($R_{\text{CR}}/l_{\text{bar}} \sim 2-3$). We attribute this to the loss of a significant fraction of the disc’s rotation during the encounter with the host galaxy.

Keywords: galaxies: dwarf — galaxies: interactions — galaxies: kinematics and dynamics — galaxies: structure

1. INTRODUCTION

Bars are among the most prominent features of disc galaxies. Their share in the galaxy population depends on the criteria employed. In the local Universe bars are hosted by at least 25% of disc galaxies (Masters et al. 2011; Cheung et al. 2013). If one includes also weak bars, the fraction may be as high as 60%. Looking into the past, the fraction of strong bars declines, down to 10% at $z \approx 0.8$ (Sheth et al. 2008). There are some indications that the number of barred galaxies may depend on the environment, in particular it may be higher in denser regions (Skibba et al. 2012; Méndez-Abreu et al. 2012). Janz et al. (2012) found that bright dwarf galaxies in the Virgo Cluster exhibit a bar fraction of 18%.

The subject of bar physics is very broad and here we recount only the most important facts. For more details, the reader can refer to recent reviews of Athanassoula (2013) and Sellwood (2014). One of the possible ways to create a barred galaxy is via global instability occurring in a cold disk. Already in the first N -body simulations it was found that discs of galaxies are often unstable (Miller et al. 1970; Hohl 1971; Ostriker & Peebles 1973; Miller & Smith 1979) and prone to the formation of a bar-like feature in their centers. From the analysis of the orbital structure of such objects Contopoulos (1980) concluded that bars should be smaller than the corotation radius R_{CR} . Athanassoula (1980), analysing response of galaxies to forcings of different extent, also

reached a similar conclusion. Later, the simulations of Athanassoula (1992a,b) confirmed this upper limit to the bar length and also added a lower limit, suggesting that the ratio of the corotation radius to the bar length $\mathcal{R} = R_{\text{CR}}/l_{\text{bar}}$ should be in a range $1 < \mathcal{R} < 1.4$. About two-thirds of galaxies with determined pattern speed are fast and almost all of them exhibit $\mathcal{R} < 2$ (Corsini 2011; Font et al. 2017).

Shortly after formation, bars undergo a vertical instability called buckling (Combes & Sanders 1981; Combes et al. 1990; Raha et al. 1991). It leads to the thickening of the bar and is responsible for the development of the boxy/peanut bulges in disc galaxies (see Athanassoula 2016, for a review). Athanassoula (2002, 2003) showed that the further evolution of the bar is governed by the transfer of the angular momentum, which is emitted by the resonances in the bar region and absorbed by the resonances in the outer parts of the disc and particularly in the dark matter halo. As a result, the bar slows down and is able to grow. The formation of bars was also studied in hydrodynamical cosmological simulations (Scannapieco & Athanassoula 2012; Algorry et al. 2016).

Bars may also form in response to an interaction with a perturber, which was first studied by Noguchi (1987) and Gerin et al. (1990). Such bars seem to be similar to the ones formed in isolation, however, there are two important differences. If the

galaxy is initially sufficiently stable against spontaneous bar formation, the pattern speed of a tidally induced bar is not decreasing in a secular fashion, but remains constant (Salo 1991; Miwa & Noguchi 1998; Martínez-Valpuesta et al. 2017). Moreover, such bars are usually slow, having $\mathcal{R} \sim 2 - 3$ (Miwa & Noguchi 1998; Berentzen et al. 2004; Aguerri & González-García 2009; Lokas et al. 2014, 2016). Miwa & Noguchi (1998) argued that such values of \mathcal{R} are caused by the transfer of the angular momentum to the perturber.

Encounters between galaxies have been known for a long time to change the appearance and structure of galaxies (e.g. Toomre & Toomre 1972). Tidal force influences the evolution of galaxies in groups (Villalobos et al. 2012) and clusters (Mastropietro et al. 2005; Lokas et al. 2016; Semczuk et al. 2017). In the tidal stirring scenario, disk dwarf galaxies are transformed into dwarf spheroidals, both in the case of dwarfs around normal-size galaxies (Mayer et al. 2001; Kazantzidis et al. 2011) and in clusters (Aguerre & González-García 2009). During the first encounter with the host galaxy, a bar develops in the disc of the dwarf (Klimentowski et al. 2009). At subsequent pericenter passages the disc thickens and later on it is transformed into a spheroid.

If the tidal stirring scenario is valid, we may expect to find some dwarfs with hints of bar presence in the Local Group. There is evidence that the elongated shape of the Sagittarius, Ursa Minor and Carina dwarfs (Lokas et al. 2010, 2012; Fabrizio et al. 2016) may be the result of the bar phase they underwent during their tidal evolution. In addition, also the ultra-faint dwarfs Hercules and Ursa Major II exhibit bar-like shapes (Coleman et al. 2007; Muñoz et al. 2010). Of course, the tidally induced bars may form not only in the Local Group, but also in other dwarf galaxies interacting with their hosts. One of the possible examples is a small galaxy in the Arp 83 system (also known as NGC 3799), which seems to interact with a larger host NGC 3800.

Recently, Lokas et al. (2014) studied in detail the evolution of a tidally induced bar in a dwarf orbiting around a Milky Way-like galaxy. Here, we extend their results to different orbital configurations. The main issue we focus on is the impact of two parameters on the bar formation. We study the outcome of varying the orbit size (i.e. peri- and apocentric distances) and the inclination of the dwarf’s disc with respect to the orbit. We also draw some more general conclusions regarding tidally induced bars. The paper is organized as follows. In Section 2 we introduce our simulations. In Section 3 we describe the results. Next, in Section 4 we discuss the results and we summarize our work in Section 5.

2. SIMULATIONS

Our simulation setup resembles the one adopted by Lokas et al. (2014). We constructed N -body models of the dwarf and the host galaxy. Both consist of a spherical NFW (Navarro et al. 1995) dark matter halo, which

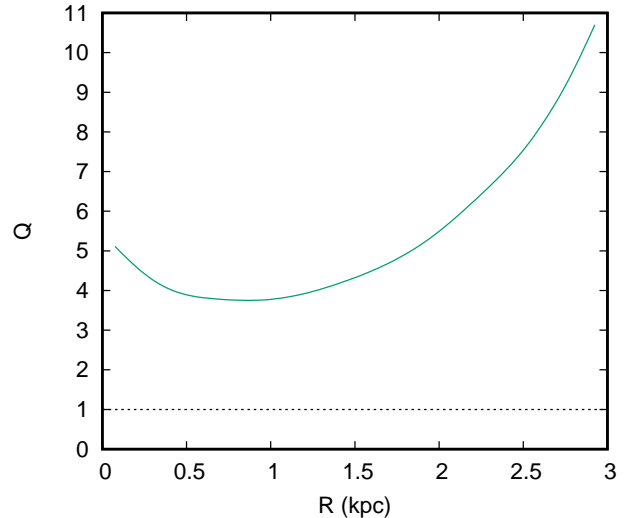


Figure 1. Initial profile of the Toomre parameter for the dwarf galaxy. The disc is stable if $Q > 1$.

Table 1. Basic properties of the simulations.

Run	Apocenter (kpc)	Pericenter (kpc)	Inclination (deg)	Line color
M0	120	24	0	Black
S0	100	20	0	Green
L0	250	50	0	Blue
M45	120	24	45	Violet
M90	120	24	90	Red

is exponentially truncated at the virial radius, and an exponential stellar disc. The models were generated using procedures described in Widrow & Dubinski (2005) and Widrow et al. (2008). Each component of each galaxy was made of 10^6 particles. According to Dubinski et al. (2009) such a number of particles is sufficient to faithfully reproduce the evolution of a barred galaxy.

To model the dwarf, we used a dark matter halo of the $10^9 M_\odot$ virial mass and a concentration of 20. The exponential stellar disc has a mass of $2 \times 10^7 M_\odot$, a radial scale-length of 0.41 kpc and a vertical scale-length of 0.082 kpc. The host galaxy was designed to resemble the Milky Way. Its dark matter halo virial mass was set to $7.7 \times 10^{11} M_\odot$ and its concentration to 27. The exponential disc has a mass of $3.4 \times 10^{10} M_\odot$, the radial scale-length is 2.82 kpc and the vertical scale-length is 0.44 kpc.

We constructed the dwarf galaxy model ensuring that it is stable against spontaneous bar formation. Toomre’s (1964) stability criterion reads

$$Q = \frac{\sigma_R \kappa}{3.36 G \Sigma} > 1, \quad (1)$$

where σ_R is the radial velocity dispersion, κ is the epicyclic frequency, Σ is the surface density of the disk and G is the gravitational constant. We plotted the initial profile of $Q(R)$ for the dwarf galaxy in Figure 1.

The minimum value is equal to 3.75, hence no bar should grow in its disk for times comparable to the evolution times considered here. We verified this by running an additional 10 Gyr simulation of the dwarf galaxy in isolation. The model of the host galaxy has a similar property, having a minimum value of $Q \approx 2$. However, the bar in the host would probably have no impact on the gravitational potential felt by the dwarf on its orbit.

We intended to gauge the impact of two factors on the bar formation: the size of the orbit of the dwarf galaxy and the inclination of its stellar disc with respect to the orbit. We chose a fiducial simulation of a pericenter 24 kpc, an apocenter 120 kpc and fully in-plane prograde orientation of the disc. It means that in the beginning the disc lies in the same plane as the orbit of the dwarf and rotates in the same direction as it orbits the host galaxy. Such an orientation maximizes the impact of the tidal interaction (Kazantzidis et al. 2011; Lokas et al. 2015). We will refer to this simulation as run M0 (where the letter ‘M’ stands for medium-size orbit and the number ‘0’ indicates the inclination angle in degrees).

In the next two runs we changed the size of the orbit, keeping the ratio of the apocenter to the pericenter distance equal to the typical values of 5, as well as the in-plane prograde orientation. In the run S0 (‘S’ for small) the orbit was tighter than M0, with the pericenter of 20 kpc and the apocenter of 100 kpc. The L0 (‘L’ for large) orbit was wider, with the pericenter at 50 kpc and the apocenter at 250 kpc.

In two other runs we varied the inclination angle of the dwarf’s disc, while keeping the same, medium, orbit size. Compared to run M0, we rotated the disc around the line connecting the initial position of the dwarf and the host center in anticlockwise direction, as viewed from the host. In run M45 we rotated the disc by 45° , while in run M90 the disc was rotated by 90° , so it was perpendicular to the plane of the orbit. The simulation runs are summarized in Table 1. We listed the designations of the runs, the apo- and pericenter distances, as well as the initial disc inclinations. In the last column we give colors, which we will use for a given simulation throughout the paper.

To give the simulations a gentle start, we always initially place the dwarfs at the apocenters of their orbits. The initial orbital velocity is set so as to reach the desired distance at the pericenter. Throughout the simulation runs, the orbits of the dwarfs do not decay significantly. The pericenter distances remain almost constant, while the apocenters decrease by less than 10%.

To run the simulations we used the publicly available code GADGET2 (Springel 2005). The evolution of the system was followed for 10 Gyr and outputs were saved every 0.05 Gyr. For the dwarf we adopted the following softening lengths: 0.02 kpc for the stellar particles and 0.06 kpc for the dark matter particles. In the case of the host galaxy, we used 0.05 kpc for the stellar component and 2 kpc for the dark matter halo.

3. RESULTS

3.1. The shape of the stellar component

In the following we will be using a reference frame aligned with the bar. The principal axes of the bar were determined through diagonalization of the inertia tensor (Zemp et al. 2011; Gajda et al. 2015), calculated for the particles inside an ellipsoid of semi-major axis length equal to 1 kpc. We rotate the reference frame in such a way that the x -axis is aligned with the major axis of the bar, the y -axis with the intermediate and the z -axis with the minor one. In this task, as well as for computing other quantities, we used the scale of 1 kpc, which is slightly smaller than our typical bar lengths. In principle, we could have used the bar length itself for this purpose, however we decided to refrain from this because it would make it difficult to disentangle the intrinsic changes of a given quantity and the variation due to the change of the bar length. Moreover, the length of the bar itself is not an easily defined quantity (Athanasoula & Misiriotis 2002).

In Figure 2 we show surface density maps of the dwarfs after their first pericenter passage (strictly speaking, at their second apocenters) and at the end of the simulations (after 10 Gyr). At the latter time, all of them are close to their next apocenter, so their shapes are not very disturbed. In all the dwarfs, bars are clearly visible after the first pericenter passage, but their lengths and shapes are different. There are no peanut shapes visible in the edge-on views, hence it seems that the dwarfs did not undergo recognizable buckling. The end products of the evolution are also diverse but in all the dwarfs the central stellar distributions remain elongated.

First, let us examine the influence of the orbit size. In the course of the simulation, the fiducial dwarf M0 became almost spherical and only its center remained elongated. Early in its life, the bar formed in dwarf S0 (on the tighter orbit) is slightly less extended than the bar in M0. At the end, the dwarf is smaller and rounder due to enhanced tidal stripping. The bar in run L0 (wider orbit) is also shorter than M0. An elongated shape visible in the face-on view at the second apocenter, inclined to the bar in the center, originates from winding up of spiral arms and will be discussed later on. This run is the only one in which the dwarf remained clearly disk-like until the end, with an easily discernible bar. It is the result of the fact that the L0 dwarf experienced only two pericenter passages.

In the case of the inclined dwarfs (M45 and M90) there is plenty of material out of the disc plane after the first pericenter. It was torn off the disc by the tidal force because both discs are inclined with respect to the plane of the orbit. The bars get shorter with growing inclination, however the final shapes of the dwarfs M45 and M90 are qualitatively similar to the M0 case.

The total amount of stripped material strongly correlates with the size of the orbit. Thus, the dwarf on the S0 orbit lost the largest amount of matter, as expected, while the one on L0 the least. The dwarfs on the same

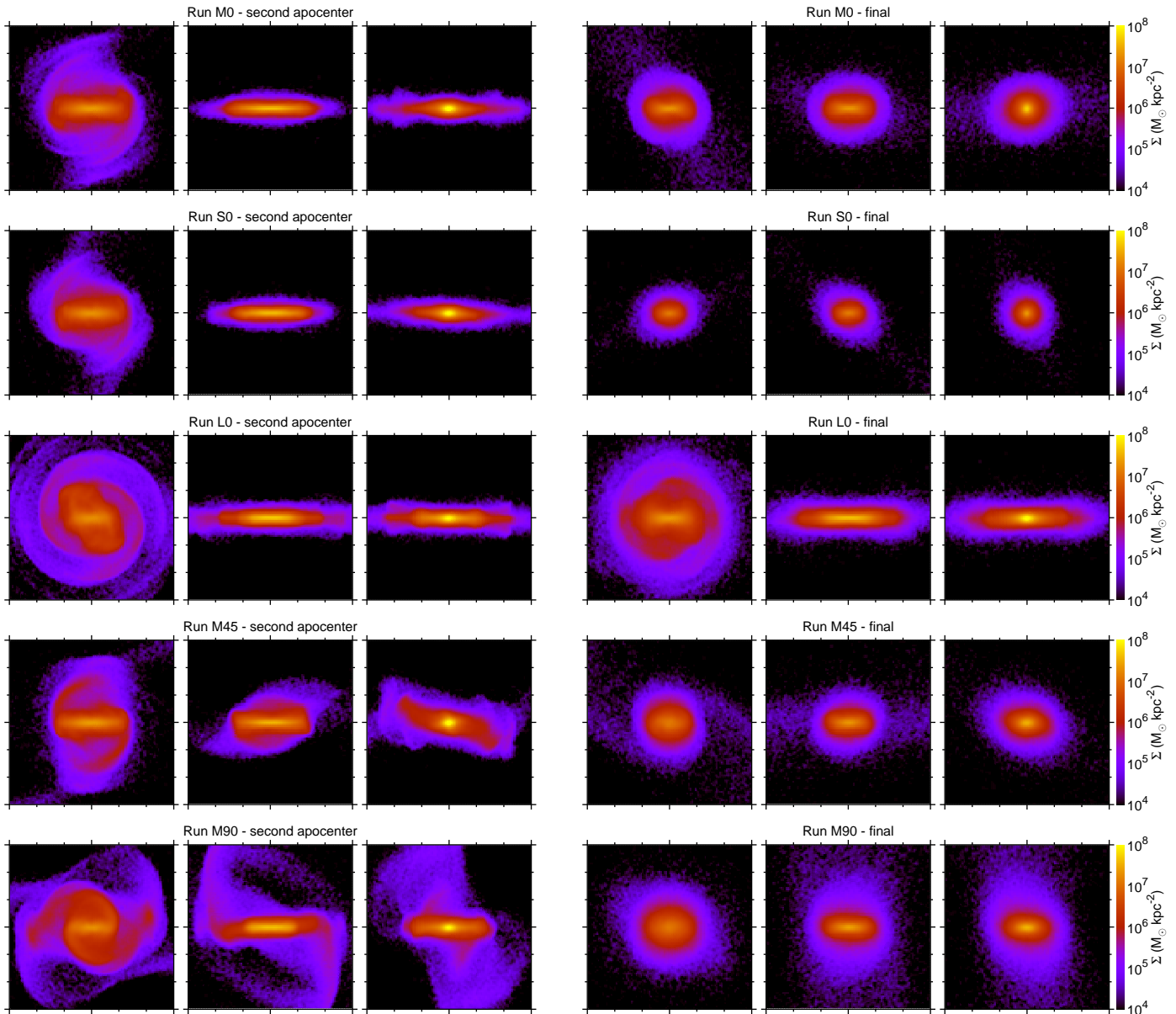


Figure 2. Surface density maps of the stellar component of the dwarf galaxies. Each row corresponds to one of the simulation runs. The set of first three columns presents the (x, y) , (x, z) and (y, z) views of the dwarfs at their second apocenter (i.e. after the first pericenter passage), respectively: the face-on, edge-on and end-on view. The second set of three columns shows the same three views, but after 10 Gyr of evolution. The side of each panel is 6 kpc. Small ticks are 1 kpc apart.

orbit (M0, M45, M90) lost a similar fraction of mass, but the trend between them is such that the fraction drops with the inclination (see also Lokas et al. 2015).

Figure 3 depicts the evolution of the dwarf stellar component shape. We quantify it in terms of the axis ratios: intermediate to major (b/a), minor to major (c/a) and minor to intermediate (c/b). In the calculations of the axis ratios we used stellar particles inside ellipsoids of semi-major axis equal to 1 kpc, hence approximately $a = 1$ kpc. This length is of the order of the bar sizes, so here we actually measure the *bar* shapes. All the dwarfs were initially axially symmetric discs ($b/a = 1$), but their shapes changed abruptly at the first pericenter passage. This hints that the bar forms in a short time at

the first pericenter, as we will show in detail in Sec. 3.3. Later on, the parameters are usually constant between pericenters. At the pericenters, the measured shape may fluctuate significantly, as can be seen especially in the case of run S0, in which there are large spikes in b/a . This is related to the fact that at pericenter the bars are not necessarily oriented along the line from the dwarf to the host, along which the tidal force acts. Thus, during the encounter with the host galaxy the tides may temporarily make the central parts of the dwarf rounder. The size of this effect depends both on the orientation of the bar and the pericenter distance.

After each pericenter the bar usually becomes less elongated, but the strength of this effect depends on the

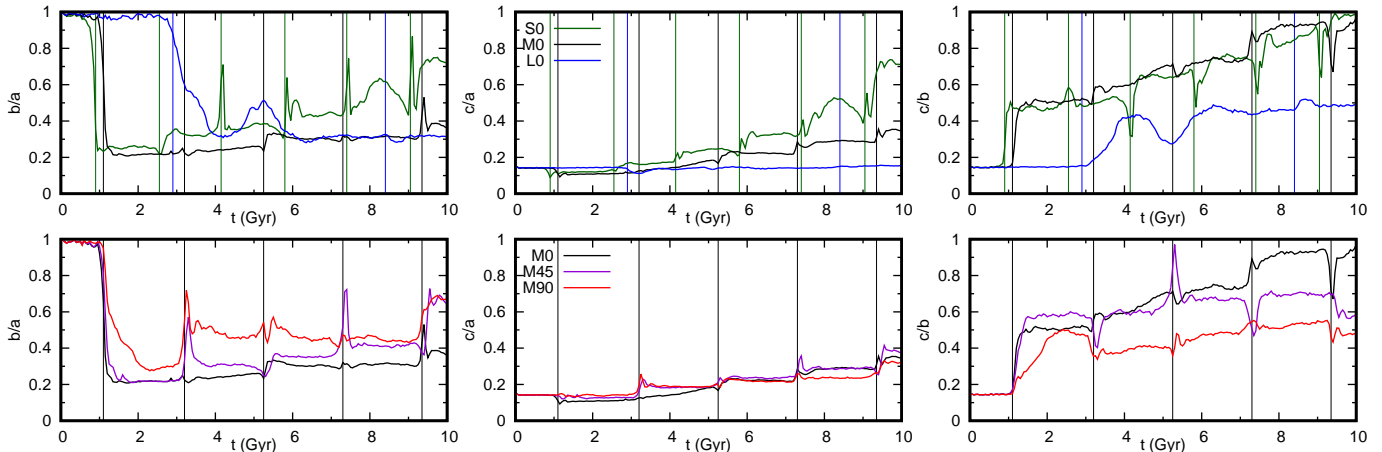


Figure 3. Axis ratios of the dwarf galaxy as a function of time. From left to right: minor to major, intermediate to major and minor to intermediate. Top row: impact of the orbit size. Bottom Row: impact of the inclination. Vertical lines indicate pericenter passages and are shown in colors corresponding to a given simulation.

size of the orbit. Also the thickness increases during the encounters with the host. Interestingly, in the M0 run, during the period between 3.5 and 5.5 Gyr, c/a grows steadily, suggesting a possible buckling episode. Upon detailed inspection of the density maps, this turned out to be true, however it was barely noticeable. We note the bars initially have $c/b \sim 0.5$, indicating they are not axisymmetric, prolate ellipsoids. However, the dwarfs S0 and M0 reach such a state at the end of the runs.

The impact of the inclination on the elongation is such that for a more inclined disk the bar is initially less elongated and remains so. On the other hand, the change in thickness (measured by c/a) is similar for all the dwarfs M0, M45, and M90.

We used the methods mentioned earlier (Zemp et al. 2011; Gajda et al. 2015) to measure how the shape of the stellar component varies with the distance from the center of the dwarf. According to Zemp et al. (2011), the axis ratios obtained by this method correspond to ellipsoidal shells of constant density. In addition to the axis ratios, to quantify the shape we also use a triaxiality parameter T , defined as

$$T = \frac{1 - (b/a)^2}{1 - (c/a)^2}. \quad (2)$$

An object with $T < 1/3$ can be considered oblate (disky) and if $T > 2/3$ it is prolate (cigar-like). For the intermediate values of T the shape is triaxial. In Figures 4 and 5 we present the axis ratios and T as a function of distance along the major axis. As in the case of the surface density maps (Figure 2), we show the results when the dwarfs were at the second apocenter and at the end of the simulations.

After the first pericenter passage the profiles of the axis ratios are qualitatively similar for all dwarfs. The discs remained thin ($c/a \approx 0.15$), with an exception of the outer parts of the inclined runs (M45 and especially M90), which is caused by the material pulled out of the disc plane by the tides. The profiles of the intermediate-

to-major ratios underwent considerable changes. In the central parts b/a dropped to ≈ 0.3 , signifying the presence of a bar. In the outskirts it grows again, but only to ≈ 0.8 , hence the discs are not fully round.

The shape evolution is well described by the triaxiality, T . In the bar region $T \approx 0.9$, as expected for an elongated bar. Further out, it drops abruptly, which corresponds to the end of the bar. However, it barely drops to $\sim 1/3$, hence the shape is not fully disk-like, but rather triaxial. The prominent exception is run L0, whose outer parts remained disk-like because of the large pericenter distance. The very central parts ($x < 0.25$ kpc) appear to be rounder than the bars. We caution that it might be the effect of insufficient resolution. An ellipsoid of major axis $a = 0.2$ kpc and $b/a = 0.3$ would have $b = 0.06$ kpc, which is only thrice the softening length of the stars and of the order of the softening of dark matter particles.

The most elongated and the longest bar developed in dwarf M0. Both smaller and larger pericenter distances lead to a shorter bar. Higher inclination of the disc also leads to bar suppression.

The shapes of the dwarf galaxies at the end of the runs are different and depend strongly on the initial conditions. In runs M0 and S0 the stellar component in the center became axisymmetric ($c/b \approx 1$), while remaining prolate. The elongated part is smaller and thicker than in the beginning, while its outskirts developed into a spherical envelope. At the end, S0 is less elongated and more axisymmetric than M0 and we can consider it to be more evolved due to a larger number of closer pericenter passages. As we have seen before, run L0 is different, with bar becoming more prominent and longer. In addition, its outer parts retained the shape of a thin disc.

In the case of the inclined discs we can see a different progression at the end of the simulations. While the thickness profiles (c/a) of runs M45 and M90 resemble the one of run M0, the ratio b/a is different. The shape in the center is considerably rounder, as indicated by

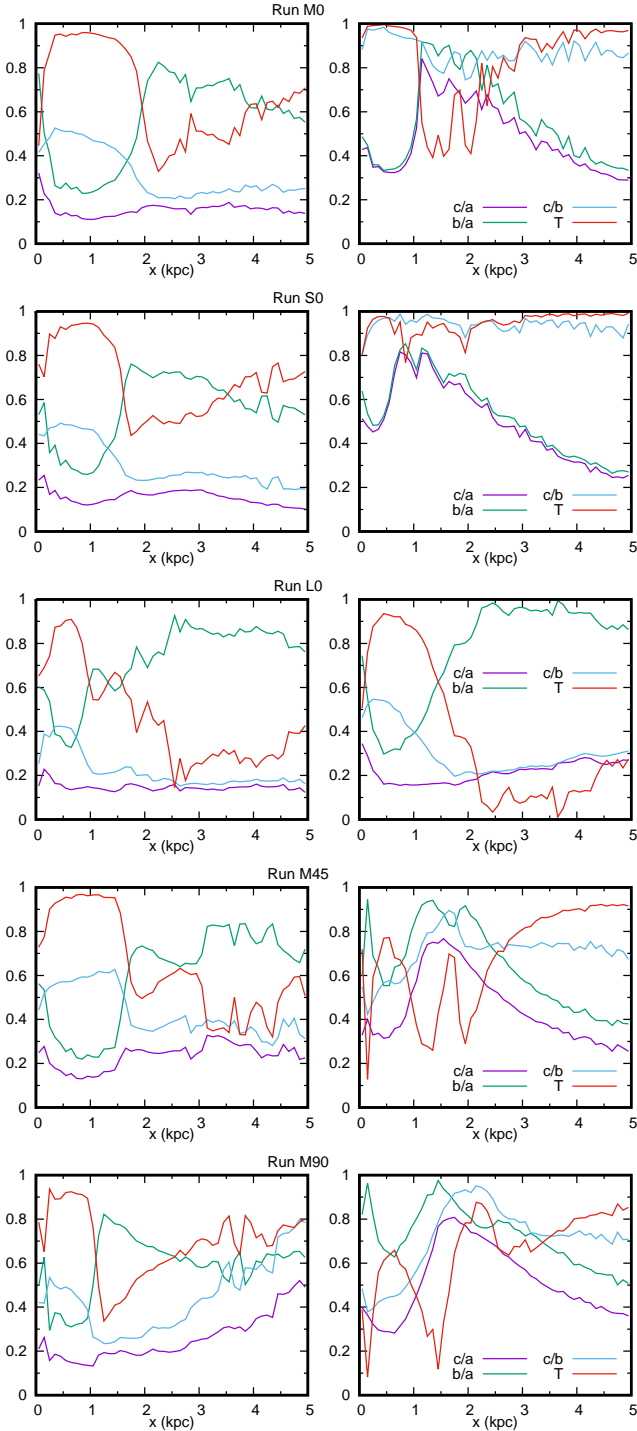


Figure 4. Shapes of the stellar component at the second apocenter (left column) and at the end of the simulations (right column) as a function of distance from the center of the dwarf. Each row corresponds to a different run. The violet lines show the minor to major axis ratio (c/a), the blue ones minor to intermediate (c/b), and the green ones intermediate to major (b/a). The triaxiality parameter, T , is plotted with the red line.

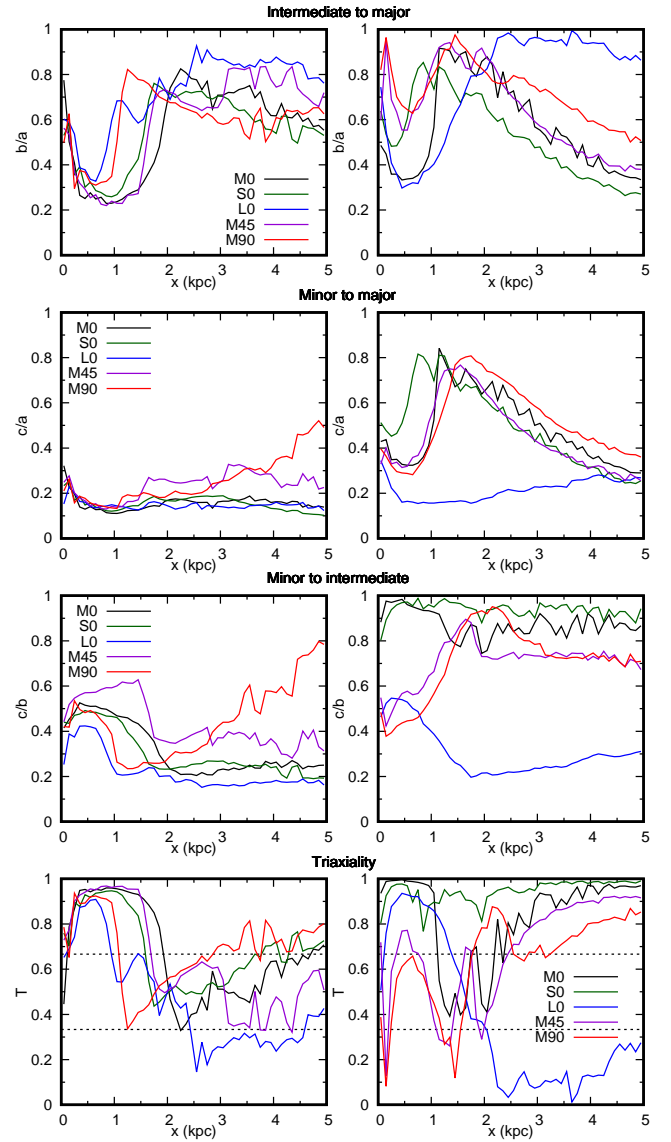


Figure 5. Shapes of the stellar component at the second apocenter (left column) and at the end of the simulations (right column) as a function of distance from the center of the dwarf. The data are the same as for Figure 4, but the layout is such as to allow comparisons between runs. From top to bottom, the rows depict intermediate-to-major, minor-to-major and minor-to-intermediate axis ratios and finally triaxiality. In the last row, dashed lines indicate ranges of prolateness ($T > 2/3$), triaxiality ($2/3 > T > 1/3$) and oblateness ($T < 1/3$). Colours of the lines correspond to the different simulation runs.

a larger b/a value. As a result, T has a smaller maximum. Actually, according to our criteria, the bar in run M90 does not have a prolate shape ($T_{\max} < 2/3$). However, the region where the distribution is elongated is distinguishable from the more spherical envelope. In most cases, T grows at large distances. This indicates the transition from the main body of the dwarf to its tidal tails, which are obviously elongated.

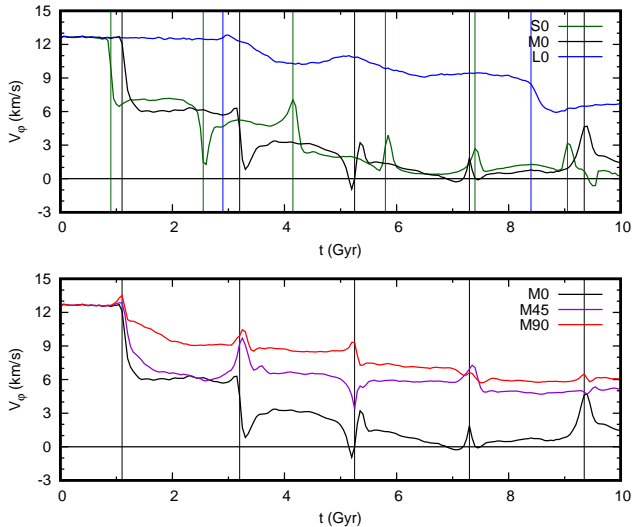


Figure 6. Evolution with time of the rotation velocity of the stellar component. Vertical lines indicate pericenter passages.

3.2. Stellar kinematics

To study the kinematics of the stellar component, we will use a spherical coordinate system including the distance from the center r , the polar angle θ and the position angle φ . In Figure 6 we show the mean rotation velocity V_φ calculated including all particles inside a 1 kpc sphere. All dwarfs lost rotation due to tidal interaction with the host galaxy. The strong decrease at the first pericenter is an effect of the bar formation inside the discs. This decrease is relatively smaller in the cases of L0 and M90 because their newly developed bars are shorter and weaker than in the other runs (see Sec. 3.3). In the course of the whole 10 Gyr of evolution, the most severe decrease took place for the dwarfs with small pericenters and in-plane prograde discs (S0 and M0). Conversely, a large pericenter or an inclined disc allowed a dwarf to retain rotation to some degree.

In Figure 7 we show the evolution of the radial velocity dispersion σ_r , measured inside 1 kpc sphere. At the first pericenter, it grows in all cases, indicating the emergence of more radial orbits, typical for bars. In some cases there are spikes of σ_r at the time of the pericenter passages, caused by strong disturbances of the dwarfs, especially in the run S0. The average value of σ_r after the first pericenter passage was largest in run M0, in which the bar is also the strongest. The later average decrease of this parameter is caused by the mass loss at subsequent pericenters passages. An exception to this trend was dwarf L0, for which σ_r grew at the second pericenter, possibly because the stripping was rather weak, allowing the bar to grow. The velocity dispersion is fairly constant between pericenters, indicating that the bar is stable at these periods of time. We checked also the dispersion of transverse velocities σ_θ and σ_φ . The evolution of σ_φ is qualitatively similar to the evolution of σ_r , only the initial growth is smaller.

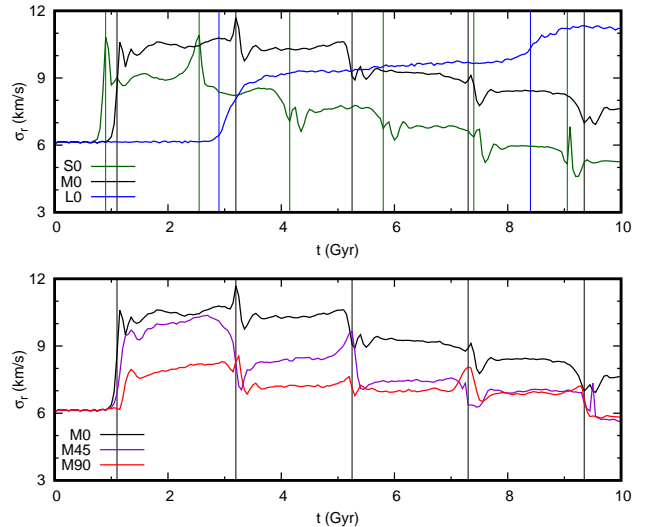


Figure 7. The radial velocity dispersion of the stars, σ_r , measured inside 1 kpc, as a function of time. Vertical lines indicate pericenter passages.

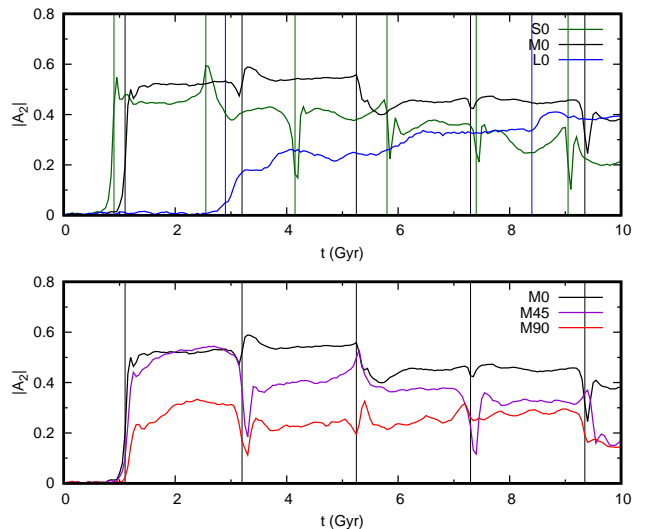


Figure 8. The bar mode $|A_2|$ measured inside 1 kpc as a function of time. Vertical lines indicate pericenter passages.

The σ_θ velocity dispersion is initially small and it grows later on. In the case of S0 both are almost identical in the end.

3.3. Properties of the bars

Now we are turning to specific diagnostics of the bar itself. To quantify the bar strength we are going to use the so-called *bar mode*

$$A_2 = \frac{1}{N} \sum_{j=1}^N \exp(i 2\varphi_j), \quad (3)$$

where the summation runs over all stellar particles in the region of interest, i is the imaginary unit and φ_j is the position angle of the j -th particle. The bar strength is given by $|A_2|$, whereas its position angle by $\arg(A_2)/2$.

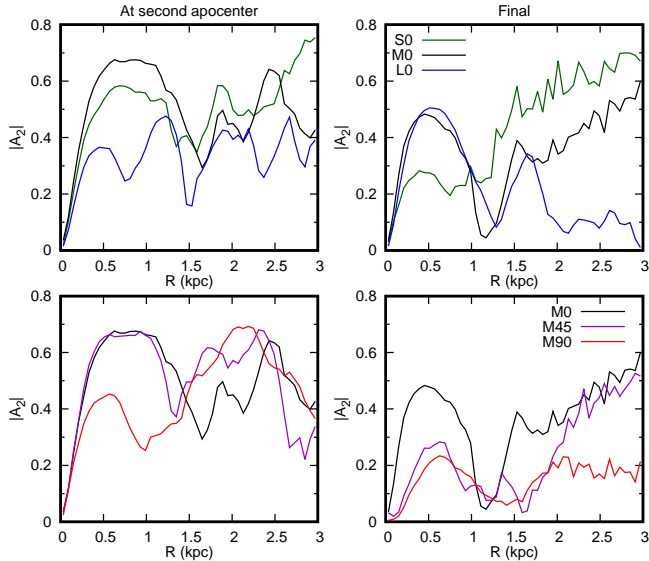


Figure 9. The bar mode $|A_2|$ profiles at the second apocenter (left column) and at the end of the simulations (right column).

We calculated A_2 for all stars inside a cylinder of 1 kpc radius, centered on the dwarf galaxy. The results are presented in Figure 8. The bar mode grows abruptly at the first pericenter passage when all the bars develop. Subsequent pericenters may strengthen the bar a little, however in most cases they become weaker after each encounter with the host galaxy.

Regarding the impact of the size of the orbit, the strongest bar is formed for the default orbit M0. The smaller pericenter distance of S0 does not lead to a stronger bar. This may be due to a shorter time of the interaction or a stronger disturbance of the disc. Later on, the S0 bar is weakened at each pericenter. The bar in the dwarf L0, on much wider orbit, is born much weaker, however it gets stronger during the second pericenter passage. The mildly inclined M45 hosts initially a bar as strong as M0, but afterwards it is weakened more. The bar in M90 dwarf is not as strong as in M45, but until the fifth pericenter passage its $|A_2|$ is constant or even slightly growing.

In Figure 9 we show the radial profiles of $|A_2|$ after the first pericenter passage and at the end of the simulation runs. Obviously, the innermost peaks correspond to the bars themselves. However, the overall profile shapes are significantly more complicated than in the case of the bars formed in isolation, for which $|A_2|$ falls down and remains low in the outskirts (e.g. Athanassoula & Misiriotis 2002). Here we have structures of larger amplitudes in the profiles. The peaks occurring away from the centers are related to rings, spiral arms or shells of matter travelling outward. The noisy increase of $|A_2|$ at the outskirts of the dwarfs, especially at the final stages, is caused by the low-density tidal tails formed by the stripped material.

In Figure 10 we illustrate how the radial profiles of $|A_2|$

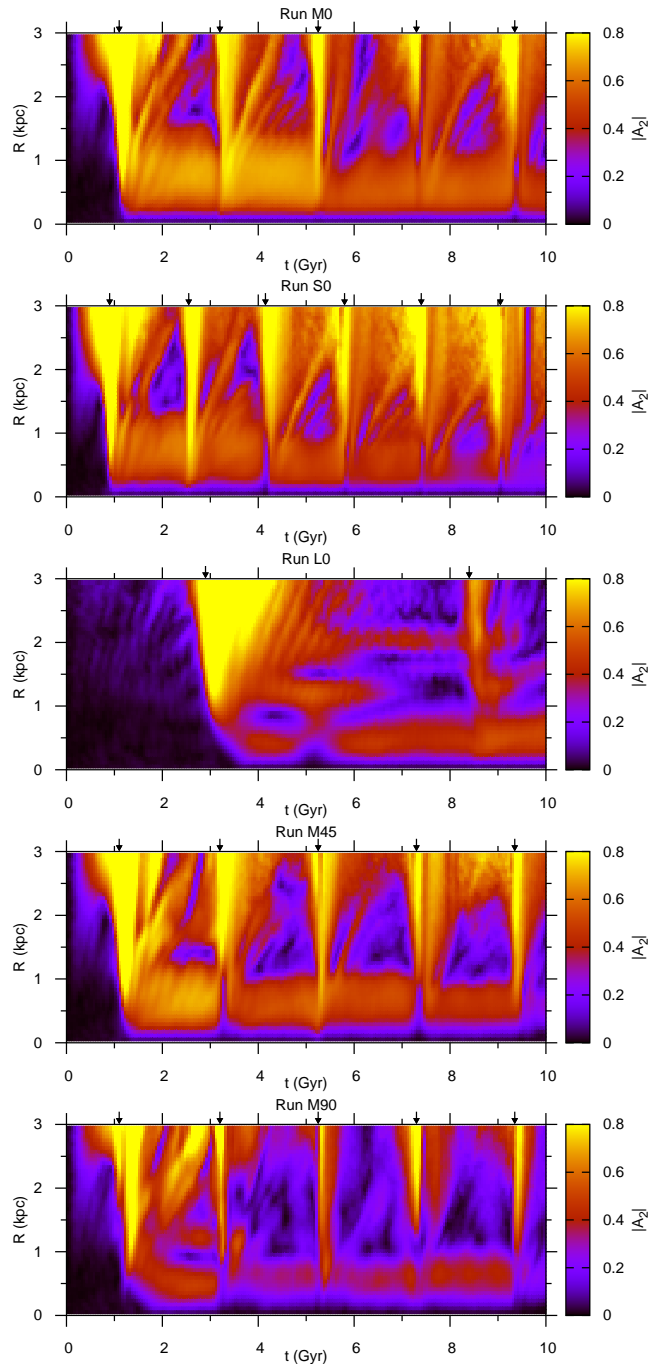


Figure 10. The bar mode $|A_2|$ versus time and distance from the dwarf’s center. Small arrows above the plots indicate the pericenter passages. Note that at those times the outer regions are saturated (i.e. $|A_2| > 0.8$).

evolve with time. One can immediately notice the pericenter passages at which the outer parts of the dwarfs are strongly stretched. In all cases bars form after the first pericenter, as indicated by the emergence of $|A_2|$ maxima at the scales of 0.5–1 kpc. The profiles of $|A_2(r)|$ does not evolve significantly in between pericenters, as can be also inferred from the global measurement in Figure 8. One can also notice narrow $|A_2|$ maxima travelling outward. We inspected the relevant density maps

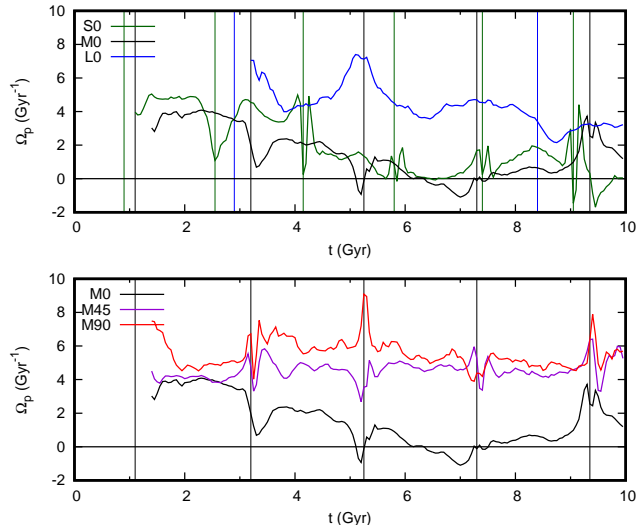


Figure 11. Pattern speed Ω_p of the bar as a function of time. The curves start when the bars are fully formed.

and concluded that these are shells of matter or density waves, which were pulled out during the close encounter with the host.

Out of the three in-plane prograde runs with differing orbit sizes, the longest and strongest bar is formed in run M0 with the intermediate pericenter distance. In runs M0 and S0 the bar is getting weaker and shorter at each pericenter. The dwarf S0 is severely stripped, as indicated by yellowish color beyond ≈ 1.5 kpc at 8.5 Gyr. In that region, only some stellar particles remain, forming elongated tidal tails. On the other hand, in L0 the bar actually gets stronger at the second pericenter passage. Examining the dependence of bar properties on the orientation of the disc, we note a clear progression that the more inclined the disc, the weaker the bar is.

We would like to calculate the bar pattern speed Ω_p . Unfortunately, the discs of the dwarfs are precessing, especially in run M45, so that we cannot simply compare position angles of the bar at two outputs. There are at least two possible approaches to solve this issue. The first one involves construction of appropriate matrix operator representing transformation of the galaxy principal axes between two outputs. The bar rotation angle can be obtained from the components of this matrix. In the second approach one can associate the initial and final orientations of the vector normal to the disc plane and the bar with four points on a unit sphere. The angle we are seeking can be found by means of spherical trigonometry. We decided to take the former approach and the details of the construction are described in Appendix A. We checked that the results obtained with the second method are the same. In fact, in our simulations the precession rates are small. Thus, our precise measurements are not very different from results which can be obtained with some approximate method, such as measuring the 3D angle between the initial and final orientation of the bar.

We cannot use in our method the principal axes com-

puted in Sec. 3.1, because some of the bars are initially shorter than 1 kpc. Instead, we use the z -axes from Sec. 3.1 (which correspond to the direction normal to the disc plane) and compute the bar orientation from the phase of A_2 , calculated using particles inside cylinders of radius 0.5 kpc. To measure the pattern speed at the time of the output n , we compare the principal axes between the outputs $n - 1$ and $n + 1$.

The evolution of Ω_p is presented in Figure 11. Each curve starts shortly after the first pericenter passage, when the bar is fully formed. Soon after formation all bars have a similar pattern speed of ~ 4 Gyr $^{-1}$, however the detailed hierarchy corresponds to the reversed order of strength, as could have been expected from previous studies (Athanasoula 2003). Later on we can observe short-term variation, especially at the pericenter passages, when the bars are highly distorted and A_2 is dominated by the elongation due to the proximity of the host. The tidal force also exerts a torque on the bar, as discussed by Lokas et al. (2014), which may affect the bar rotation in the vicinity of the pericenter. We verified that the changes of the pattern speed are not driven by the mass loss. The evolution of both stellar and dark matter mass in the bar region is very similar for the three dwarfs on the same orbit (M0, M45 and M90), yet their Ω_p varies differently.

Apart from short-timescale fluctuations, we notice also long-term trends. In case of the in-plane prograde dwarfs on small-pericenter orbits (S0 and M0), bars are significantly slowing down and finally halt after a few pericenters. Interestingly, the bar in run M0 temporarily reverses its rotation speed around 7 Gyr. On the other hand, the slowdown is more gradual in L0 and M90 runs. In M45 the pattern speed appears to be on average constant. In all cases, the evolution of Ω_p has trends similar to those of the mean rotation velocity change shown in Figure 6.

The most obvious property of a bar is its length. Athanasoula & Misiriotis (2002) discussed various methods to estimate it. We note there is no method to measure the bar size unambiguously and many of them require setting some *ad hoc* parameters. We decided to employ a method inspired by the aforementioned paper. We define the bar semi-major axis length as the distance from the center where triaxiality T obtained from our algorithm drops below 90% of its maximal value. We motivate this choice by the fact that T profiles are quite flat in the center and further outside drop steeply. Our selected threshold intends to reflect this drop.

In Figure 12 we depicted the evolution of the bar lengths. We note that at some outputs we were unable to determine l_b . The typical reason was that the dwarfs at pericenters, or shortly afterwards, were so disturbed that our method did not work, mainly because T grew all the way from the center to the outskirts. As was the case for many other properties discussed so far, l_b is quite stable between pericenters, while it usually changes after each pericenter passage. Hence, the bars

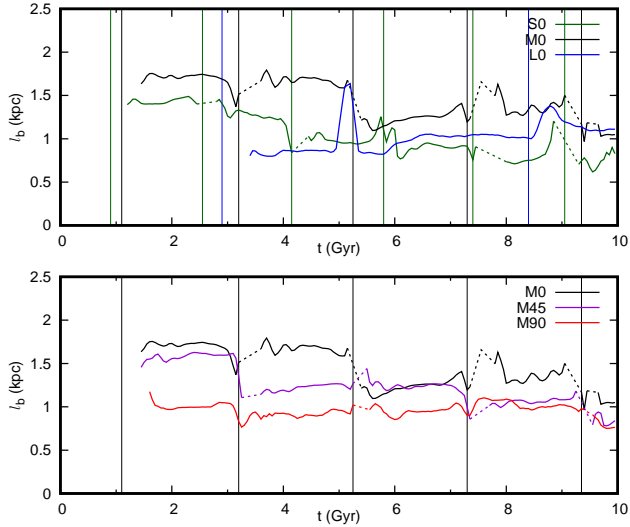


Figure 12. The bar length l_b , measured from the drop in triaxiality, as a function of time. To smooth the results, we applied a moving average over three consecutive outputs. Dashed parts of the lines correspond to periods when the bar length determination was not possible. The vertical lines indicate pericenter passages.

do not undergo significant secular evolution.

The longest bar was formed in dwarf M0, whereas in runs with smaller (S0) and larger (L0) orbit size the bar was initially shorter. Furthermore, there is a trend with disc inclination, such that for a larger one the bar is shorter. However, the evolution of l_b is not very easy to predict. For example, sometimes the M45 bar has the length equal to the one of M0, but at other instances equal to the one of M90. We note that at the end of simulations (except for L0) the dwarfs should be regarded as having elongated central parts, surrounded by spheroidal envelope, rather than as a disc with a bar component. The sudden increase and then decrease of L0 bar length around 5 Gyr is caused by the winding up of spiral arms and corresponds to an elongated feature visible in Figure 2.

3.4. Dynamics of the bar rotation

An important parameter for the bar dynamics is a ratio of the corotation radius to the bar length $\mathcal{R} = R_{\text{CR}}/l_b$. The corotation radius R_{CR} is defined as $\Omega_{\text{circ}}(R_{\text{CR}}) = \Omega_p$, where $\Omega_{\text{circ}}(R)$ is the circular velocity of the galaxy.

A careful analysis of possible orbits in bars by Contopoulos (1980) showed that bars must follow the relation $R_{\text{CR}} > l_b$ (i.e. $\mathcal{R} > 1$). A similar conclusion was reached by Athanassoula (1980), who used forcings of different extents but found that bars were always shorter than the corotation radius. This limit to the bar length can be illustrated by a following simplified reasoning. Most of the stellar particles in the bar are on prograde orbits (i.e. they orbit around the dwarf center faster than the bar rotates). However, the velocity of the particles at apocenters cannot be larger than the circular velocity. The pattern speed of the bar is the same

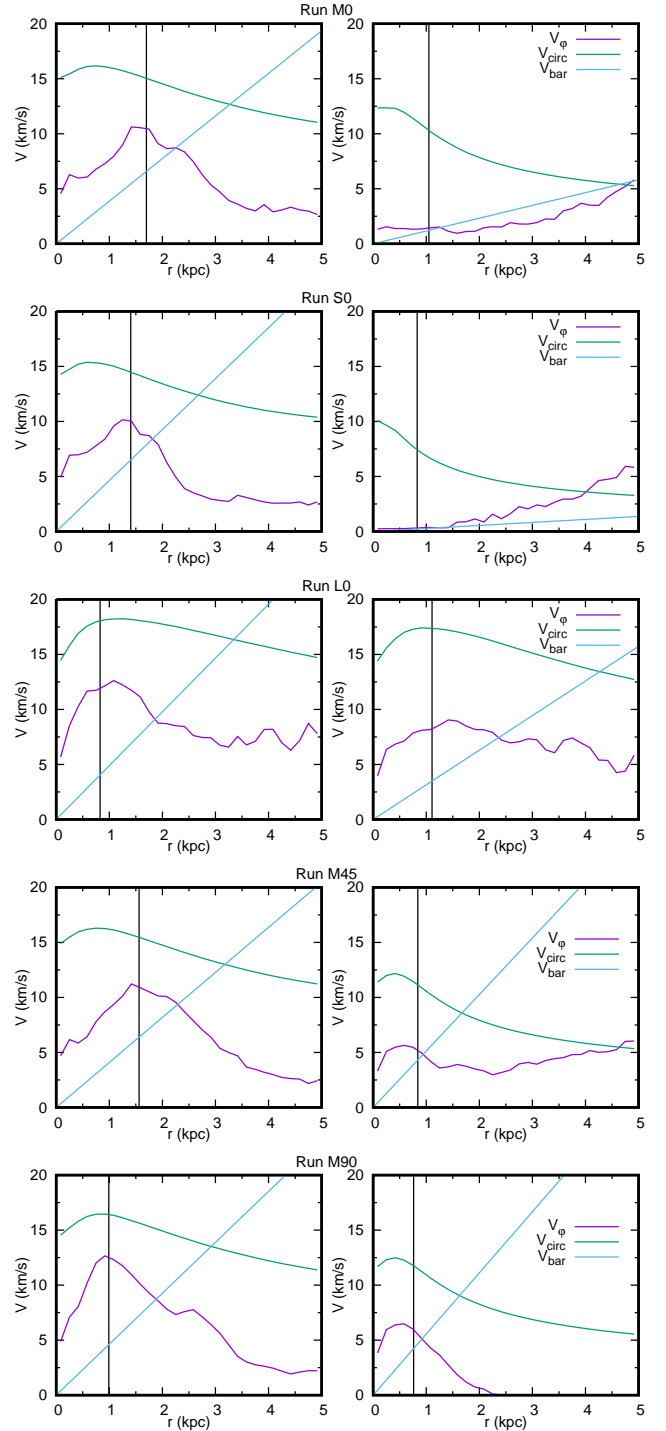


Figure 13. The circular velocity V_{circ} (green), the true rotation velocity V_ϕ (violet) and the bar speed at a given distance $V_{\text{bar}} = r\Omega_p$ (blue). Vertical lines indicate the bar length l_b . Left column depicts the second apocenter and the right column the final state.

at every radius, hence the bar must end before circular angular speed drops below it, meaning that we expect $R_{\text{CR}} > l_b$.

Bars with $\mathcal{R} < 1.4$ are considered *fast*, because their pattern speed is close to the maximal possible rotation speed at a given bar length. Conversely, bars for which

$\mathcal{R} > 1.4$ are called *slow*. In general, N -body simulations indicate that bars formed in isolation tend to be fast and indeed have $1 < \mathcal{R} < 1.4$ (see Athanassoula 2013). However, this may depend to some extent on the choice of initial parameters as slow bars have also been shown to form in isolation (Lokas et al. 2016). Bars formed in interactions are rather slow (e.g. Miwa & Noguchi 1998).

We analyzed in detail the rotation in the dwarfs. However, we present it in terms of the rotation velocity instead of angular speed, because this way highlights more features. In Figure 13 we plotted the circular velocity V_{circ} , the true rotation velocity of the stellar component V_{φ} and the linear bar rotation velocity $V_{\text{bar}} = R\Omega_{\text{p}}$. We computed the circular velocity as

$$V_{\text{circ}}(R) = \left[\frac{GM(r < R)}{R} \right]^{1/2}, \quad (4)$$

where G is the gravitational constant, r is the distance from the center and $M(r < R)$ is the total mass (both baryonic and dark) closer to the dwarf's center than R . We calculated V_{φ} by averaging particle velocities at a given distance. The bar length is also indicated in each panel.

The much lower values of V_{circ} at the end of simulations are the effect of mass stripping, mainly of the dark matter component. The growth of V_{φ} in the outskirts, visible in some panels, is related to the transition to the tidal arms. In some cases (e.g. at the end of run S0) V_{φ} is larger than V_{circ} . This is not surprising, as particles located in that region are already stripped from the dwarf galaxy and their movement is governed by the potential of the host. The sizes of the dwarfs can be estimated from Figure 2 and at the end of the simulations are smaller than 2 kpc (except L0, which is larger). The particles already stripped from the dwarf can move with a significant relative velocity (Lokas et al. 2013).

The maximum of the initial rotation velocity curve was around 19.4 km s^{-1} , attained approximately 2 kpc from the center. As already discussed (see Figure 6), in all cases the dwarfs lost a significant fraction of rotation, especially in the outer parts, but also in the centers. The loss of rotation is caused of course by the tidal force and stripping. The shapes of $V_{\varphi}(R)$ are qualitatively similar for all our simulations, usually with a distinct maximum. Interestingly, the measured bar lengths fall in the vicinity of these maxima. However, recall that measuring l_{b} involves a free parameter, hence it may be only a coincidence.

The values of \mathcal{R} can be obtained by finding the intersection of V_{bar} and V_{circ} (blue and green) curves and comparing them to the bar length. We conclude that all our bars are slow, having values of \mathcal{R} from 2 to 4 and more. However, considering the true rotation velocity V_{φ} (violet lines), we see that the bars are actually rotating quite fast compared to the rotation velocity of the stars. By similar argument as above, bars are limited by the *true corotation*, i.e. the radius where the pattern speed is the same as the actual angular velocity of the

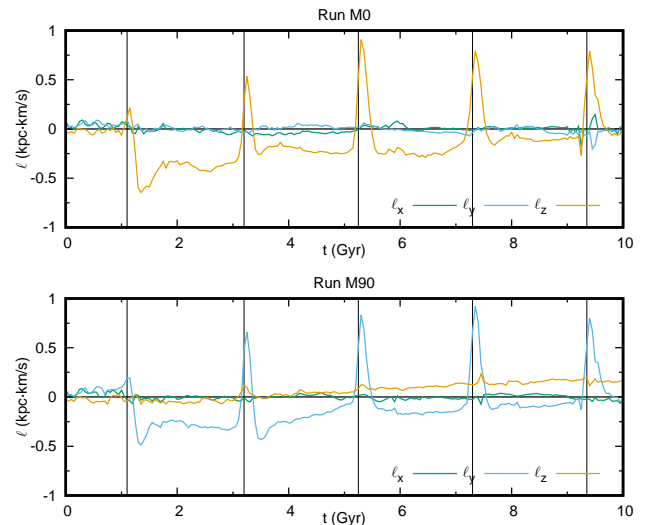


Figure 14. The specific angular momentum ℓ of the central parts of the dark matter haloes in simulations M0 and M90 (see text) as a function of time. Here the reference frame is such that the initial angular momentum of the disc is along the z axis. In such a frame, the orbital angular momentum of dwarf M0 is also along the z axis, but in run M90 it is along the y axis (i.e. the dwarf orbits in the xz plane).

stars.

Out of the in-plane prograde dwarfs, the slowest (in terms of \mathcal{R}) is the bar in run L0, which is caused by its short length. However, one has to remember that if we consider the periods after the first pericenters, this bar is actually *the fastest* in terms of Ω_{p} . For the inclined dwarfs, \mathcal{R} drops with inclination, but here again M90 is the fastest in terms of the pattern speed. Hence one has to be careful, since bars may be fast according to one definition and at the same time slow according to another (see also Font et al. 2017).

At the end of the simulations, in the two in-plane prograde dwarfs with small pericenters (M0 and S0) the bars are very slow, as they are barely rotating. The dwarfs with inclined discs retained their pattern speed (see Figure 11) and at the same time they lost rotation and a lot of mass, hence they are actually faster than at the second apocenter.

3.5. Angular momentum transfer

An important concept in the studies of barred galaxies is the angular momentum transfer. It is quite well established that in the case of simulations of isolated galaxies the bars emit angular momentum, which is absorbed by their dark matter haloes. This process enables bars to grow in the secular evolution phase. We intended to study this process in the case of our simulations. Unfortunately, the stellar component loses a large fraction of its amount of angular momentum via tidal interactions with the host galaxy directly to the tidal tails, and this leads to the decrease of rotation in the whole disc. Thus, any bar-related evolution of angular momentum was obscured by this process.

We were, however, able to track the behavior of the

angular momentum of the dark matter halo. To study this effect, we use a reference frame different from the one used previously. Now the z axis is placed along the initial axis of rotation of the disc and the axes are kept constant. In Figure 14 we show the time evolution of the specific angular momentum ℓ of the central parts of dark matter haloes in two examples, M0 and M90. In the calculation we take into account all particles closer than 2 kpc from the centers of the dwarfs. Recall that in run M0 the dwarf was on the in-plane prograde orbit, hence the z axis is also perpendicular to the initial orbital plane. In run M90 the disc was perpendicular to the orbital plane, so the z axis lies *in* this plane. The axis perpendicular to the plane is denoted as y . The angular momentum evolution in runs S0 and L0 is qualitatively similar to run M0. In run M45 the disc is precessing significantly, making the relevant plot incomprehensible.

The most prominent feature in both panels of Figure 14 is the variation of angular momentum component along the axis of the orbital motion (z in run M0 and y in run M90). After the first pericenter both halos acquire negative (i.e. retrograde) angular momentum. This is a direct result of the preferential stripping of particles on prograde orbits, in contrast to the retrograde ones (Hénon 1970; Gajda & Lokas 2016, and references therein). The spikes appearing just after the pericenter passages are due to the disturbance by the tidal force. In run M90 we can observe small, but steady increase of the ℓ_z component, resulting from the angular momentum transfer. In the case of run M0, such an increase in ℓ_z is buried under larger changes induced by tides. Most of the angular momentum lost by the stellar component is not transferred to the dark matter halo of the dwarf galaxy.

4. DISCUSSION

4.1. *Buckling instability and thickening*

Buckling instability is a common phase of bar evolution. In the case of bars formed in isolation, it usually takes place soon after the bar formation. The instability leads to a change in the velocity distribution of the galaxy. Obviously, the vertical velocity dispersion σ_z grows, but also the in-plane dispersion, e.g. σ_R , decreases (e.g. Martínez-Valpuesta & Shlosman 2004). It has been argued (see Binney & Tremaine 2008, and references therein) that a critical parameter for the instability is the ratio of σ_z/σ_R .

To check whether the dwarfs underwent buckling instability we investigated edge-on surface density maps. In runs M45, M90 and L0 we did not detect any significant vertical asymmetry at any time. On the other hand, dwarf M0 underwent buckling and in run S0 we also detected some weak traces of possible instability. Traces of undergoing buckling in run M0 can be noticed in the c/a measurement in Figure 3, where it grows steadily between 3 and 5 Gyr. Moreover, σ_θ grows at the same time.

The occurrence of buckling in the simulations may be related to the strength of the individual bars. Dwarf M0 had the strongest bar, with the highest level of velocity dispersion σ_r . The bar in run S0 was slightly weaker and in run L0 was significantly weaker, at least after the first pericenter passage. This relation between the thickening amplitude and bar strength is supported by the correlation in Athanassoula (2008) and the simulations of Martínez-Valpuesta et al. (2017), among which a discernible boxy/peanut bulge is present only in the case of the most disturbed galaxy with the strongest bar. In the case of the inclined dwarfs, buckling might have been inhibited by the vertical disturbance of the disc during the pericenter passages.

One more reason why our bars did not experience strong buckling, might have been repeated pericenter passages. The dwarf galaxies were tidally shocked at each of them and the resulting disturbance might have reduced the buckling amplitude. Moreover, we cannot rule out that in cases where we did not notice the instability it actually occurred but was too weak or too fast to be recognized. None of our dwarfs formed a boxy/peanut bulge, which is usually associated with the buckling instability. Interestingly, Erwin & Debattista (2013) found that about 13% galaxies in their sample do not show signs of boxy/peanut structures. Moreover, the fraction of galaxies hosting a boxy/peanut bulge is lower for the less massive systems (Erwin & Debattista 2017).

4.2. *Tidally induced spiral arms*

We would like to point out the development of spiral arms in our simulations, provided the tidal force is not too strong. In run L0 we observe two sets of two-fold tightly wound spiral arms, both of which can be seen as distinct maxima in the relevant panel of Figure 10. The first one is located at ≈ 1.3 kpc and exists for a period of 4-6 Gyr. The second is located at ≈ 2 kpc and persists between 5-8 Gyr. Tightly wound spiral arms are also present in our run M90 ($r \approx 1.2$ kpc, $t \approx 2.5$ -3 Gyr) and are probably responsible for the weakening of the bar right after the second pericenter.

The inner set of arms can be linked to the peculiar features of L0 run around 5 Gyr, such as peaks in the pattern speed (Figure 11) and the bar length (Figure 12). Judging from the surface density maps, at this time the spiral arms seem to wind up and weaken the bar. They detach from the bar ends and finally turn into a ring around the bar, which can be seen in Figure 2. A similar structure can be also seen in some large spirals.

The reader can refer to Semczuk et al. (2017) for a detailed study of tidally induced spiral arms, albeit in the context of normal-size galaxies orbiting in a galaxy cluster.

4.3. *Angular momentum and corotation*

Angular momentum and its transfer play an important role in the development and evolution of bars, as

concluded from works concerning bars formed through instability. However, in the case of tidally induced bars the angular momentum budget is different. The galaxies encounter perturbers one or more times and lose large amounts of angular momentum. Moreover, their outer parts are heavily disturbed and stripped.

Bars in isolated galaxies grow by emission of the angular momentum from inside the corotation radius, which is absorbed by the halo and the outer part of the disc (Athanasoula 2003). In our simulations R_{CR} is usually located in the outer part of the disk. In particular, after the first pericenter $R_{\text{CR}} \sim 3$ kpc, whereas initially 90% of the disc mass is inside 1.7 kpc and the radius of 3 kpc encompasses 99% of the disc mass. Therefore, there was insufficient amount of disc mass to absorb the angular momentum. In addition, our disc is initially hot and stable against bar formation. Athanasoula (2003) found that the hotter the disc the slower the deceleration of the bar.

In isolated galaxies, resonances of the dark matter halo can absorb angular momentum (Athanasoula 2003). However, haloes in our simulations are heavily stripped at all radii and heavily perturbed. On the fiducial orbit, the size of the halo drops from 6 kpc after the first pericenter to 3 kpc at the end, as can be estimated from the break in the dark matter density profile (see Figure 1 in Gajda & Lokas 2016). Moreover, the halos lose mass also from the inner parts. Almost 60% of the initial mass inside 3 kpc is lost at the first pericenter and more than 90% before the end of the simulation. In addition, we can imagine that the velocity distribution is perturbed, which may hamper angular momentum transfer (Athanasoula 2003).

The bars formed through rapid instability are usually fast, having $\mathcal{R} < 1.4$ (i.e. $l_{\text{bar}} > 0.7R_{\text{CR}}$), which means that their length almost fills the corotation radius. Tidally induced bars however, are much slower and/or shorter. Figure 13 makes it easy to understand, at least in the case of dwarf galaxies and strong tidal forces. During the interaction, the rotation velocity $V_{\varphi}(R)$ drops significantly, e.g. by a factor of 2. Hence, the bar cannot rotate as fast as in the isolated case. If we consider the *true corotation* (i.e. radius at which $V_{\varphi}/R = \Omega_{\text{p}}$), then the bars appear to rotate almost as fast as possible, given their environment.

We note that some bars formed in isolation may be slow (Villa-Vargas et al. 2009; Lokas et al. 2016; gas-poor examples of Athanasoula 2014), possibly due to the lack of gas (including during the bar formation period), to a dominant dark matter halo, or when the corotation is outside the disc. We would like to note that very slow pattern speeds, with an \mathcal{R} ratio of the order of 3, have been actually observed in at least one case of a real galaxy (Elmegreen et al. 1998), while \mathcal{R} ratios of the order of 2 are fairly common (see Font et al. 2017, and references therein).

Interestingly, the bar lengths in our simulations fall close to the maximum of the rotation curve and we can-

not offer any explanation for this, it may be only an accident. However, it would be interesting to check how this relation looks in bars formed via instability and in less perturbed tidally induced bars. It might be possibly related to the results of Lynden-Bell (1979).

4.4. Comparison with other works

Now we would like to put our work in perspective of earlier findings. First we are going to compare our bars to bars formed in isolation and then to other works on tidally induced bars.

We would like to stress that the evolution of bars in our simulation is different than in the case of bars formed through instability. In the latter, bars usually start growing soon after the beginning of the simulation, then they experience buckling instability and finally they continue growing in a secular fashion (see Athanasoula 2013, for a review). Here, the initial model of the dwarf galaxy is constructed in such a way that it is stable against spontaneous bar formation, at least over the timescales considered here (i.e. 10 Gyr). The bars develop during the first encounter with the host galaxy. Later, however, they seem not to grow in a secular way, but rather keep their parameters constant between pericenter passages. Usually, the repeated encounters with the host galaxy weaken the bars. The only exception is the L0 dwarf on the widest orbit, for which the tidal force is relatively weak.

The profiles of the bar amplitude $|A_2|$ are also different with respect to bars formed in isolation. In the latter case there is usually only a wide peak in the center, followed by a drop to near zero in the outskirts (e.g. Athanasoula 2002, 2003). The tidally induced bars may exhibit many peaks in $|A_2|$ profiles. Some of them correspond to tidally induced spiral arms, other result from shells of matter. Finally, $|A_2|$ grows in the outskirts, indicating the transition from the main body of the galaxy to its tidal tails.

Lokas et al. (2016) analyzed a suite of simulations following a Milky Way-like galaxy orbiting in a galaxy cluster. Their model of the progenitor galaxy was unstable to spontaneous bar formation, however, it needed a long time to start developing the bar on its own. In their simulations the apparent influence of the tidal force was much weaker than in our simulations, as can be judged from the $|A_2|$ enhancement at pericenter passages or the tidal radius estimates. Consequently, the initially formed bars are weaker than in our simulations. However, later on they grow continually, both during subsequent pericenter passages and in the periods between them. The Lokas et al. (2016) bars do experience buckling instability, leading to the formation of boxy/peanut shapes in edge-on views, contrary to our models.

Janz et al. (2012) found a bar fraction of 18% among early-type dwarf galaxies in the Virgo cluster. This may seem at odds with our simulations, in which all of the dwarfs developed bars. However, there are various reasons why we do not observe 100% bar fraction. Firstly,

presence of gas in real galaxies hampers bar formation (Athanasoula et al. 2013). Secondly, Smith et al. (2015) showed that in the case of galaxy clusters, dwarf galaxies need to plunge deep into the cluster core to be influenced significantly by the tidal forces. Thirdly, bars in our simulations are weakened or even destroyed during the evolution. As can be inferred from Figure 2, some of the dwarfs may not be classified as barred at final stages of their evolution, especially in case of unfavourable orientation. Last but not least, we should note that all our simulations have the same mass model. Thus the fact that they all form bars cannot be compared to the observed fraction of bars in dwarf galaxies, whose mass models span a considerable parameter space.

5. SUMMARY

The purpose of this work was to study the formation and evolution of tidally induced bars in dwarf galaxies orbiting a Milky Way-like host. We constructed an N -body model of a dwarf galaxy and verified that in isolation it is stable against bar formation over the time ranges of relevance here. In order to induce bar formation, we put the dwarf galaxy on an elongated orbit around an N -body model of a galaxy resembling the Milky Way. We focus on two parameters governing the evolution: the size of the dwarf’s orbit and its disc inclination with respect to the orbital plane. We conducted five simulations. Three of them had an in-plane prograde orientation of the disk but varying orbit sizes. For the medium-sized orbit we performed two additional simulations with the dwarf’s disc inclined by 45° and 90° with respect to the orbital plane.

In all cases, bars form during the first pericenter passage, however their properties and the subsequent evolution vary. The overall strongest bar was formed for the intermediate orbit and in-plane prograde disc orientation. On the tighter orbit the tidal force is stronger and the disc is disturbed excessively, inhibiting the formation of a strong bar. On the wider orbit the tidal forces are too weak, hence initially only a weak bar develops. In comparison to a in-plane prograde orbit, for the higher inclinations the bars are progressively weaker. In the retrograde case, Lokas et al. (2015) found that no bar forms at all. The dependence on the disc orientation stems from the progressively weaker tidal force in the equatorial plane of the dwarf and the unfavorable orientation of the Coriolis force.

The bars formed in our simulations were slow ($\mathcal{R} \sim 2 - 3$), in contrast to the bars developed in isolation, which are typically classified as fast ($\mathcal{R} < 1.4$). We found that this is caused by the loss of a huge fraction of the dwarf galaxy angular momentum during the pericenter passage, as initially proposed by Miwa & Noguchi (1998). Consequently, the stellar component of the dwarf was rotating much slower than the maximum allowed by the circular velocity. Hence, the bars were rotating significantly slower than the maxima deduced

from the comparison of their lengths to their circular velocity curves.

The life of bars developed in isolation usually includes phases of buckling and secular evolution. Here, even if a bar underwent buckling, it was only very weak. One possible reason is that the bars were weaker than in the isolated cases (Athanasoula 2008). We also did not observe noticeable secular evolution, which usually involves the bar growth and slowdown. The possible explanation is the combination of repeated tidal shocks and stripping, which hindered the angular momentum transfer.

The bars were stable between pericenter passages and evolved mainly during them. Except for the case of the widest orbit, during subsequent encounters with the host the bars were weakened and shortened. In addition, the in-plane prograde dwarfs on the tightest and the intermediate orbit quickly lost almost all of their rotation. The final states of those dwarfs consisted of an elongated central part, with some rotation possible, enshrouded in a more spheroidal envelope. Such an evolution was envisaged by the tidal stirring scenario for the transformation of a disc into a spheroid (Mayer et al. 2001; Kazantzidis et al. 2011). Obviously, it is not the buckling which leads to this thickening, but rather tidal shocking.

The main concern regarding the applicability of this work to the dwarf galaxies e.g. in the Local Group is whether the initial conditions of the simulations correspond to real systems prior to accretion into the neighborhood of a larger galaxy. Dwarf galaxies observed far away from other galaxies often possess significant amount of rotating interstellar gas. However, it remains an open question if their stellar components have structures of rather thin discs rotating in an ordered fashion, as we assumed here. Moreover, in reality the satellites are accreted from the cosmic web, whereas here we just placed the dwarfs at apocenters of their orbit and gave them appropriate speed to reach the desired pericenter. Furthermore, we neglected entirely the gas component and performed fully collisionless simulations. We know that the collisional component impacts immensely the formation and evolution of bars in isolation (Athanasoula 1992b; Villa-Vargas et al. 2010; Athanasoula et al. 2013; Athanasoula 2014) and that in fact isolated dwarf galaxies contain a large gas fraction (Papastergis et al. 2012; Sales et al. 2015). Although the gas is probably efficiently ram-pressure stripped by the hot halo of the host, it may remain in the dwarf long enough to significantly affect the evolution. We intend to study the influence of the interstellar medium on the formation of tidally induced bars in a future work.

This work was partially supported by the Polish National Science Centre under grant 2013/10/A/ST9/00023. EA is partially supported by the CNES (Centre National d’Études Spatiales,

France).

APPENDIX

A. CALCULATION OF THE PATTERN SPEED

The purpose of this appendix is to solve the following problem. At an initial time, normalised vectors \mathbf{x}_i , \mathbf{y}_i and \mathbf{z}_i point along bar principal axes, respectively, major, intermediate and minor. Similarly, vectors \mathbf{x}_f , \mathbf{y}_f and \mathbf{z}_f correspond to a later state of this galaxy, which we will hereafter refer to as the final state of the galaxy. We would like to give a proper definition of the angle ω by which the bar rotated around the minor axis and to calculate its value in terms of \mathbf{x}_i , \mathbf{y}_i , \mathbf{z}_i and \mathbf{x}_f , \mathbf{y}_f , \mathbf{z}_f .

We note that all the vectors we discuss in this appendix are normalised to unity. For purposes of matrix operations, vectors should be understood as columns consisting of three numbers.

Without loss of generality, we can choose a reference frame whose axes lie along principal axes of the bar at the initial time, i.e. $\mathbf{x}'_i = \hat{\mathbf{x}}$ and so forth. In such a frame, the final principal axes can be expressed as

$$\mathbf{x}'_f = \begin{pmatrix} \mathbf{x}_i^\top \\ \mathbf{y}_i^\top \\ \mathbf{z}_i^\top \end{pmatrix} \mathbf{x}_f, \quad (\text{A1})$$

where $^\top$ stands for transposition, so the first object on the right-hand side should be understood as a matrix, whose rows are given by components of \mathbf{x}_i , \mathbf{y}_i and \mathbf{z}_i . Similar expressions can be written for \mathbf{y}'_f and \mathbf{z}'_f . The transformation of $\{\mathbf{x}'_i, \mathbf{y}'_i, \mathbf{z}'_i\} = \{\hat{\mathbf{x}}, \hat{\mathbf{y}}, \hat{\mathbf{z}}\}$ set into $\{\mathbf{x}'_f, \mathbf{y}'_f, \mathbf{z}'_f\}$ can be described in terms of a matrix \mathbf{T} such that

$$\mathbf{T}\mathbf{x}'_i = \mathbf{T}\hat{\mathbf{x}} = \mathbf{x}'_f, \quad (\text{A2a})$$

$$\mathbf{T}\mathbf{y}'_i = \mathbf{T}\hat{\mathbf{y}} = \mathbf{y}'_f, \quad (\text{A2b})$$

$$\mathbf{T}\mathbf{z}'_i = \mathbf{T}\hat{\mathbf{z}} = \mathbf{z}'_f, \quad (\text{A2c})$$

We will seek a relation between \mathbf{T} and ω .

Let us introduce the following notation: $\mathbf{R}(\mathbf{k}, \phi)$ will be a matrix, which is an operator rotating vectors about unit vector \mathbf{k} by angle ϕ in counter clockwise direction. Elements of such a matrix can be found using the Rodrigues' rotation formula:

$$\mathbf{R}(\mathbf{k}, \phi) = \mathbf{I} + \mathbf{K} \sin \phi + \mathbf{K}^2 (1 - \cos \phi), \quad (\text{A3})$$

where \mathbf{I} is the identity matrix and \mathbf{K} is a following matrix

$$\mathbf{K} = \begin{pmatrix} 0 & -k_z & k_y \\ k_z & 0 & -k_x \\ -k_y & k_x & 0 \end{pmatrix}. \quad (\text{A4})$$

Matrix $\mathbf{R}(\mathbf{k}, \phi)$ can be viewed as an active transformation, as we described above, but as well as a passive one. Namely, it corresponds to a change of reference frame, such that the frame is rotated about \mathbf{k} by an angle $-\phi$.

From construction, \mathbf{R} is an orthogonal matrix and its inverse equals to $\mathbf{R}(\mathbf{k}, \phi)^{-1} = \mathbf{R}(\mathbf{k}, \phi)^\top = \mathbf{R}(\mathbf{k}, -\phi)$.

We need to make an assumption regarding the trajectory of the bar minor axis. This is required because otherwise we would not be able to determine a ‘‘zero-point’’ of the bar rotation angle. In particular, if the path of \mathbf{z} was unrestricted and the bar was not rotating, it could have any orientation at the final time. We assume the simplest possibility, namely that the bar minor axis follows the shortest path between $\hat{\mathbf{z}}$ and \mathbf{z}'_f . It can be regarded as a good approximation, if the outputs from the simulations are dense enough. Hence, the transformation for \mathbf{z} is following:

$$\mathbf{z}'_f = \mathbf{R}(\mathbf{n}, \theta)\hat{\mathbf{z}}, \quad (\text{A5})$$

where $\mathbf{n} = \frac{\hat{\mathbf{z}} \times \mathbf{z}'_f}{|\hat{\mathbf{z}} \times \mathbf{z}'_f|}$ and $\theta = \arccos(\hat{\mathbf{z}} \cdot \mathbf{z}'_f) = \arccos(\mathbf{z}_i \cdot \mathbf{z}_f)$.

One natural possibility for the full transformation matrix is $\mathbf{T} = \mathbf{R}(\mathbf{n}, \theta)\mathbf{R}(\hat{\mathbf{z}}, \omega)$, i.e. first we rotate about $\hat{\mathbf{z}}$ by ω and then about \mathbf{n} by θ . However, there is another possibility, namely $\mathbf{R}(\mathbf{z}'_f, \omega)\mathbf{R}(\mathbf{n}, \theta)$, i.e. first we rotate about \mathbf{n} by θ and then about \mathbf{z}'_f by ω . It turns out they are equivalent, as can be seen considering an operation $\mathbf{A} = \mathbf{R}(\mathbf{n}, \theta)\mathbf{R}(\hat{\mathbf{z}}, \omega)\mathbf{R}(\mathbf{n}, -\theta)$. It can be regarded as composition of (i) rotation of the reference frame by θ about \mathbf{n} , which sets the z -axis along \mathbf{z}'_f (ii) rotation around new z -axis and (iii) rotation of the reference frame back to the original position. Hence, it is obvious that in fact $\mathbf{A} = \mathbf{R}(\mathbf{z}'_f, \omega)$, from which follows that $\mathbf{R}(\mathbf{n}, \theta)\mathbf{R}(\hat{\mathbf{z}}, \omega) = \mathbf{R}(\mathbf{z}'_f, \omega)\mathbf{R}(\mathbf{n}, \theta)$. It can be also checked through tedious, but straightforward calculation of the elements of the matrices.

Using the above equality, we can think about the whole transformation as composed of infinitesimal rotations about \mathbf{n} , followed by rotation around the instantaneous z -axis, repeated until the final state is reached. Hence, \mathbf{T} can be thought of as

$$\mathbf{T} = \prod_{j=0}^{N-1} \mathbf{R}(\mathbf{n}, \theta/N)\mathbf{R}(\mathbf{z}_j, \omega/N), \quad (\text{A6})$$

where $\mathbf{z}_j = \mathbf{R}(\mathbf{n}, \theta/N)^j \hat{\mathbf{z}} = \mathbf{R}(\mathbf{n}, \theta j/N) \hat{\mathbf{z}}$.

The general structure of the matrix $\mathbf{T} = \mathbf{R}(\mathbf{n}, \theta)\mathbf{R}(\hat{\mathbf{z}}, \omega)$ is complicated, however combination of its elements takes a simple form

$$\mathbf{T}_{21} - \mathbf{T}_{12} = (1 + \cos \theta) \sin \omega. \quad (\text{A7})$$

Moreover, $\mathbf{T}_{33} = \cos \theta$. Hence, the rotation angle ω can be obtained from the numerical representation of \mathbf{T} using

$$\omega = \arcsin \left(\frac{\mathbf{T}_{21} - \mathbf{T}_{12}}{1 + \mathbf{T}_{33}} \right). \quad (\text{A8})$$

Let us now turn to the determination of \mathbf{T} from the initial and final orientation of the bar principal axes. Combining the definitions in (A2) we get

$$(\mathbf{x}'_f \ \mathbf{y}'_f \ \mathbf{z}'_f) = \mathbf{T}(\hat{\mathbf{x}} \ \hat{\mathbf{y}} \ \hat{\mathbf{z}}) = \mathbf{T} \quad (\text{A9})$$

Hence, the columns of \mathbf{T} are given by components of \mathbf{x}'_f , \mathbf{y}'_f and \mathbf{z}'_f . We can further substitute the expression for \mathbf{x}'_f from (A1) and similarly for \mathbf{y}'_f and \mathbf{z}'_f . Finally,

$$\mathbf{T} = \begin{pmatrix} \mathbf{x}_i^\top \\ \mathbf{y}_i^\top \\ \mathbf{z}_i^\top \end{pmatrix} (\mathbf{x}_f \ \mathbf{y}_f \ \mathbf{z}_f). \quad (\text{A10})$$

From the above form one can easily read the appropriate components of \mathbf{T} , obtaining

$$\omega = \arcsin \left(\frac{\mathbf{y}_i \cdot \mathbf{x}_f - \mathbf{x}_i \cdot \mathbf{y}_f}{1 + \mathbf{z}_i \cdot \mathbf{z}_f} \right). \quad (\text{A11})$$

The orientation of the intermediate axis can be expressed using $\mathbf{y} = \mathbf{z} \times \mathbf{x}$. Thus, the above result can be rewritten as

$$\omega = \arcsin \left(\frac{(\mathbf{z}_i + \mathbf{z}_f) \cdot (\mathbf{x}_i \times \mathbf{x}_f)}{1 + \mathbf{z}_i \cdot \mathbf{z}_f} \right). \quad (\text{A12})$$

If the disc is not precessing (i.e. $\mathbf{z}_f = \mathbf{z}_i = \mathbf{z}$), it simplifies to

$$\omega = \arcsin[\mathbf{z} \cdot (\mathbf{x}_i \times \mathbf{x}_f)], \quad (\text{A13})$$

which can be easily understood and serves as a simple check for our considerations. We see that $\omega \in [-\pi/2, \pi/2]$ is an oriented angle, which is positive if the bar rotates counter clockwise around its minor axis and negative otherwise.

REFERENCES

- Aguerri, J. A. L., & González-García, A. C. 2009, *A&A*, 494, 891
 Algorry, D. G., Navarro, J. F., Abadi, M. G., et al. 2016, arXiv:1609.05909
 Athanassoula, E. 1980, *A&A*, 88, 184
 Athanassoula, E. 1992a, *MNRAS*, 259, 328
 Athanassoula, E. 1992b, *MNRAS*, 259, 345
 Athanassoula, E. 2002, *ApJL*, 569, 83
 Athanassoula, E. 2003, *MNRAS*, 341, 1179
 Athanassoula, E. 2008, in: *Mapping the Galaxy and Nearby Galaxies*, ed. K. Wada & F. Combes (Berlin: Springer), 47
 Athanassoula, E. 2013, in: *Secular Evolution of Galaxies*, ed. J. Falcón-Barroso & J. H. Knapen (Cambridge, UK: Cambridge University Press), 305
 Athanassoula, E. 2014, *MNRAS*, 438, L81
 Athanassoula, E. 2016, in: *Galactic Bulges, Astrophysics and Space Science Library*, Vol. 418, ed. E. Laurikainen, R. Peletier, & D. Gadotti (Berlin:Springer), 391
 Athanassoula, E., Machado, R. E. G., & Rodionov, S. A. 2013, *MNRAS*, 429, 1949
 Athanassoula, E., & Misiriotis, A. 2002, *MNRAS*, 330, 35
 Berentzen, I., Athanassoula, E., Heller, C. H., & Fricke, K. J. 2004, *MNRAS*, 347, 220
 Binney, J., & Tremaine, S. 2008, *Galactic Dynamics* (2nd ed.; Princeton, NJ: Princeton Univ. Press)
 Cheung, E., Athanassoula, E., Masters, K. L., et al. 2013, *ApJ*, 779, 162
 Coleman, M. G., de Jong, J. T. A., Martin, N. F., et al. 2007, *ApJL*, 668, 43
 Combes, F., Debbasch, F., Friedli, D., & Pfenniger, D. 1990, *A&A*, 233, 82
 Combes, F., & Sanders, R. H. 1981, *A&A*, 96, 164
 Contopoulos, G. 1980, *A&A*, 81, 198
 Corsini, E. M. 2011, *MSAIS*, 18, 23
 Dubinski, J., Berentzen, I., Shlosman, I. 2009, *ApJ*, 697, 293
 Elmegreen, B. G., Wilcots, E., & Pisano, D. J. 1998, *ApJL*, 494, 37
 Erwin, P., & Debattista, V. P. 2013, *MNRAS*, 431, 3060
 Erwin, P., & Debattista, V. P. 2017, *MNRAS*, 468, 2058
 Fabrizio, M., Bono, G., Nonino, M. et al. 2016, *ApJ*, 830, 126
 Font, J., Beckman, J. E., Martnez-Valpuesta, I., et al. 2017, *ApJ*, 835, 279
 Gajda, G., & Lokas, E. L. 2016, *ApJ*, 819, 20
 Gajda, G., Lokas, E. L., & Wojtak, R. 2015, *MNRAS*, 447, 97
 Gerin, M., Combes, F., & Athanassoula, E. 1990, *A&A*, 230, 37
 Hénon, M. 1970, *A&A*, 9, 24
 Hohl, F. 1971, *ApJ*, 168, 343
 Janz, J., Laurikainen, E., Lisker, T., et al. 2012, *ApJL*, 745, 24
 Kazantzidis, S., Lokas, E. L., Callegari, S., et al. 2011, *ApJ*, 726, 98
 Klimentowski, J., Lokas, E. L., Kazantzidis, S., et al. 2009, *MNRAS*, 397, 2015
 Lynden-Bell, D. 1979, *MNRAS*, 187, 101
 Lokas, E. L., Kazantzidis, S., Majewski, S. R., et al. 2010, *ApJ*, 725, 1516
 Lokas, E. L., Majewski, S. R., Kazantzidis, S., et al. 2012, *ApJ*, 751, 61
 Lokas, E. L., Gajda, G., & Kazantzidis, S. 2013, *MNRAS*, 433, 878
 Lokas, E. L., Athanassoula, E., Debattista, V. P., et al. 2014, *MNRAS*, 445, 1339
 Lokas, E. L., Semczuk, M., Gajda, G., & D'Onghia, E. 2015, *ApJ*, 810, 100
 Lokas, E. L., Ebrova, I., del Pino, A., et al. 2016, *ApJ*, 826, 227
 Martinez-Valpuesta, I., Aguerri, J. A. L., González-García, A. C., et al. 2017, *MNRAS*, 464, 1502
 Martinez-Valpuesta, I., & Shlosman, I. 2004, *ApJL*, 613, 29
 Masters, K. L., Nichol, R. C., Hoyle, B., et al. 2011, *MNRAS*, 411, 2026
 Mastropietro, C., Moore, B., Mayer, L., et al. 2005, *MNRAS*, 364, 607
 Mayer, L., Governato, F., Colpi, M., et al. 2001, *ApJ*, 559, 754
 Méndez-Abreu, J., Sánchez-Janssen, R., Aguerri, J. A. L., et al. 2012, *ApJL*, 761, 6
 Miller, R. H., Prendergast, K. H., & Quirk, W. J. 1970, *ApJ*, 161, 903
 Miller, R. H., & Smith, B. F. 1979, *ApJ*, 227, 785
 Miwa, T., & Noguchi, M. 1998, *ApJ*, 499, 149
 Muñoz, R. R., Geha, M., & Willman, B. 2010, *ApJ*, 140, 138
 Navarro J. F., Frenk C. S., & White S. D. M. 1995, *MNRAS*, 275, 720
 Noguchi, M. 1987, *MNRAS*, 228, 635
 Ostriker, J. P., & Peebles, P. J. E. 1973, *ApJ*, 186, 467
 Papastergis, E., Cattaneo, A., Huang, S., et al. 2012, *ApJ*, 759, 138
 Raha, N., Sellwood, J. A., James, R. A., & Kahn, F. D. 1991, *Nature*, 352, 411
 Sales, L. V., Vogelsberger, M., Genel, S., et al. 2015, *MNRAS*, 447, L6
 Salo, H. 1991, *A&A*, 243, 118
 Scannapieco, C., & Athanassoula, E. 2012, *MNRAS*, 425, 10
 Sellwood, J. A. 2014, *RvMP*, 86, 1
 Semczuk, M., Lokas, E. L., & del Pino, A. 2017, *ApJ*, 834, 7

- Sheth, K., Elmegreen, D. M., Elmegreen, B. G., et al. 2008, *ApJ*, 675, 1141
- Skibba, R. A., Masters, K. L., Nichol, R. C., et al. 2012, *MNRAS* 423, 1485
- Springel, V. 2005, *MNRAS*, 364, 1105
- Smith, R., Sánchez-Janssen, R., Beasley, M. A., et al. 2015, *MNRAS*, 454, 2502
- Toomre, A. 1964, *ApJ*, 139, 1217
- Toomre, A., & Toomre, J. 1972, *ApJ*, 178, 623
- Villalobos, Á., De Lucia, G., Borgani, S., & Murante, G. 2012, *MNRAS*, 424, 2401
- Villa-Vargas, J., Shlosman, I., & Heller, C. 2009, *ApJ*, 707, 218
- Villa-Vargas, J., Shlosman, I., & Heller, C. 2010, *ApJ*, 719, 1470
- Widrow, L. M., & Dubinski, J. 2005, *ApJ*, 631, 838
- Widrow, L. M., Pym, B., & Dubinski, J. 2008, *ApJ*, 679, 1239
- Zemp, M., Gnedin, O. Y., Gnedin, N. Y., & Kravtsov, A. V. 2011, *ApJS*, 197, 30